JGR Oceans

RESEARCH ARTICLE
10.1029/2019JC015527

Special Section:
Contributions from the Physics of Estuaries and Coastal Seas meeting, 2018

Numerical Study of the Exchange Flow of the Persian Gulf Using an Extended Total Exchange Flow Analysis Framework

Marvin Lorenz[1], **Knut Klingbeil**[1], **and Hans Burchard**[1]

[1]Leibniz Institute for Baltic Sea Research Warnemünde, Rostock, Germany

Abstract The Total Exchange Flow analysis framework computes consistent bulk values quantifying the estuarine exchange flow using salinity coordinates since salinity is the main contributor to density in estuaries and the salinity budget is entirely controlled by the exchange flow. For deeper and larger estuaries temperature may contribute equally or even more to the density. That is why we included potential temperature as a second coordinate to the Total Exchange Flow analysis framework, which allows gaining insights in the potential temperature-salinity structure of the exchange flow as well as to compute consistent bulk potential temperature and therefore heat exchange values with the ocean. We applied this theory to the exchange flow of the Persian Gulf, a shallow, semienclosed marginal sea, where dominant evaporation leads to the formation of hypersaline and dense Gulf water. This drives an inverse estuarine circulation which is analyzed with special interest on the seasonal cycle of the exchange flow. The exchange flow of the Persian Gulf is numerically simulated with the General Estuarine Transport Model from 1993 to 2016 and validated against observations. Results show that a clear seasonal cycle exists with stronger exchange flow rates in the first half of the year. Furthermore, the composition of the outflowing water is investigated using passive tracers, which mark different surface waters. The results show that in the first half of the year, most outflowing water comes from the southern coast, while in the second half most water originates from the northwestern region.

Plain Language Summary We studied the water exchange of the Persian Gulf with the Indian Ocean through the Strait of Hormuz. Due to evaporation, fresh water is removed in the Gulf but the salt of the water stays behind. This process creates hypersaline, thus dense water, which flows as a bottom current into the Indian Ocean. We performed a numerical simulation from 1993 to 2016, which we compared to observations and other model studies. Using the simulation's results, we could show that the water exchange follows a seasonal cycle with varying water properties, that is, salinity and temperature. Volume exchange is found to be stronger in the first half of the year than the second. The inflowing water has a nearly constant salinity but varies strongly in temperature. The salinity and temperature of the outflowing water are dependent on the origin of the water. Dense water, formed in fall and early winter in the southern Arabian coast, leaves the Gulf in late winter and spring. Dense water formed in the north at the same time arrives in the Strait of Hormuz in summer and fall. This change in origin can be found as a signature of colder and more saline outflowing water.

Key Points:
- The Total Exchange Flow analysis framework was extended by including potential temperature, which yields T-S diagrams of the exchange flow
- We conducted a 24-year simulation of the Persian Gulf using GETM
- We applied the extended TEF analysis framework to the simulation and analyzed the seasonality of the exchange flow

Supporting Information:
- Supporting Information S1

Correspondence to:
M. Lorenz,
marvin.lorenz@io-warnemuende.de

Citation:
Lorenz, M., Klingbeil, K., & Burchard, H. (2020). Numerical study of the exchange flow of the Persian Gulf using an extended Total Exchange Flow analysis framework. *Journal of Geophysical Research: Oceans*, *125*, e2019JC015527. https://doi.org/10.1029/2019JC015527

Received 26 JUL 2019
Accepted 8 JAN 2020
Accepted article online 16 JAN 2020

The copyright line for this article was changed on 7 JUL 2020 after original online publication.

1. Introduction

Estuarine exchange flows can be described with simple yet precise bulk values (Knudsen, 1900), for residual volume fluxes, Q_{in} and Q_{out}, and bulk salinities s_{in}, s_{out}.The Total Exchange Flow (TEF) analysis framework (MacCready, 2011) offers a consistent calculation of the Knudsen bulk values using salinity coordinates instead of spatial coordinates since the salt budget is entirely controlled by the exchange flow. It successfully combined the concept of continuous salinity coordinates (Walin, 1977) with the bulk value concept of Knudsen (1900). Despite the bulk values, the other main result of TEF is profiles of the volume transport in salinity space, which provides a detailed insight in the salinity structure of the exchange flow. A numerically accurate and general computation of the bulk values from the TEF profiles has been discussed in Lorenz et al. (2019). Additionally, the bulk values were recently used to quantify estuarine mixing, defined as the destruction of salinity variance in estuaries (MacCready et al., 2018; Burchard et al., 2019).

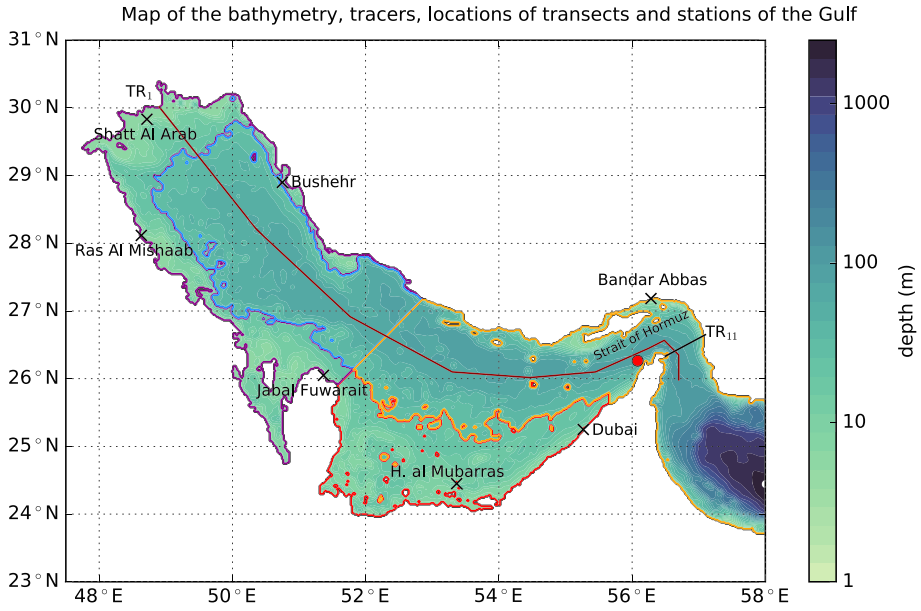

Figure 1. Map of the model domain and bathymetry of the Gulf. We marked different regions of the Gulf with different surface tracers when the water last was in contact with the atmosphere (colored contours). Tracer 1 (red) marks the shallow (<30 m) southern coast, Tracer 2 the shallow northern coast (purple), Tracer 3 the deeper northeastern part (blue), and Tracer 4 the central and western part (orange). Furthermore, the transects and stations used in this paper are marked: transects (along the Gulf axis: TR_1 and in the Strait of Hormuz: TR_{11}), tidal stations (black crosses), position of data from Johns et al. (2003) (red dot).

Whereas previous studies focused on freshwater dominated estuaries, we apply the TEF analysis framework in this study to the exchange flow of the Persian Gulf (also known as Arabian Gulf), an inverse estuary with dominating evaporation, to investigate the seasonality. With winter water temperatures below 20 °C and summer water temperatures above 35 °C (Alessi et al., 1999; Reynolds, 1993) the Gulf is heavily impacted by the seasonal solar radiation. For this purpose we extended TEF to include potential temperature space. This allows the decomposition of the potential temperature-salinity structure of the exchange flow (sections 2 and 4.1). This extended method is applicable to any estuarine exchange flow and allows the user to estimate the heat exchange through any transect. Similar decompositions have been applied to stream functions in the open ocean and to study water mass transformation processes (Döös et al., 2012; Groeskamp et al., 2019; Hieronymus et al., 2014; Speer, 1993; Worthington, 1981; Zika et al., 2013). The Gulf is a semienclosed marginal sea, connected through the Strait of Hormuz to the Gulf of Oman and Arabian Sea. The Gulf itself is shallow (mean depth of 39 m), consists of shallow coastal regions in the north and south, and has a deeper trench following the axis of the Gulf along the Iranian coast to the Strait of Hormuz; compare Figure 1. Very high Gulf-wide-averaged evaporation rates, up to 2 m/a and locally even more (Ahmad & Sultan, 1991; Privett, 1959), exceed the precipitation, resulting in the creation of hypersaline Persian Gulf Water (PGW) and drive an inverse estuarine circulation. PGW is leaving the Gulf as a bottom current and Indian Ocean Surface Water (IOSW) is entering through the Strait of Hormuz to compensate the volume loss. The PGW stratifies in relatively shallow depth into the Gulf of Oman (~250 m), mixes with ambient water due to mesoscale and submesoscale eddies (Morvan et al., 2019; Vic et al., 2015), and spreads into the Indian Ocean where PGW signatures can be found, for example, in the Bay of Bengal (Jain et al., 2017). Previous measurements showed that the outflow of the PGW does not follow a significant seasonal cycle and is relatively steady with only small variabilities one time scales of 2–3 weeks (Johns et al., 2003; Swift & Bower, 2003; Pous et al., 2004).

Other and more recent model studies find a seasonal cycle of weaker outflows in winter and stronger outflows in summer (Chao et al., 1992; Elhakeem et al., 2015; Kämpf & Sadrinasab, 2006; Pous et al., 2015; Yao & Johns, 2010b). In addition, the measurements of Johns et al. (2003) show episodic salinity pulses in the outflow from March to July 1997. Thoppil and Hogan (2009) investigated these pulses and showed that these are a signal of propagating mesoscale cyclonic eddies, formed in the vicinity of 26°N, 55.5°E due to

baroclinic instabilities. These are triggered by abrupt changes of the local circulation due to wind stress fluctuations. Yao and Johns (2010b) argued that longer pulses from the measurements are caused by spilling of saline water from the southern shallows.

Previous model studies that indicate a seasonality computed only inflowing and outflowing transports for monthly or annual values and described the PGW salinities by a range of minimum to maximum values. In addition, these studies did not utilize the benefits of TEF. Therefore, this study conducts an extensive analysis of the exchange flow and its properties for the climatological exchange flow as well as time series of bulk values.

Another question we want to answer is the question of the composition of the PGW. Previous studies discussed the origin of the PGW, which is known to mainly form in the north and in the south (Swift & Bower, 2003; Yao & Johns, 2010b) with highest densities found in winter in the north. The southern shallows form dense water in autumn and winter, which reaches the Strait of Hormuz in late winter and spring (Kämpf & Sadrinasab, 2006), while the water from the north is steady over the whole year (Yao & Johns, 2010b).

To provide a quantitative measure of the composition of the PGW, we conducted a tracer experiment by marking the surface waters of different regions where they were in last contact with the atmosphere. Then, we computed the composition of the outflowing water by calculating the respective concentration bulk values of the tracers. With this approach we are able to gain insights of the different composition and especially the ratio of water from northern and southern origin.

This paper is structured as following. In section 2 we provide a summary of the TEF computation and the extension of potential temperature as the second coordinate. In section 3 the model and the setup description are presented in detail including the validation of the model. The results of this study are shown in section 4, starting in section 4.1 with an example for the potential temperature-salinity TEF, before showing the results of the application on the Gulf. Discussion of the results is done in section 5 before we summarize and conclude in section 6.

2. Methods

2.1. TEF Analysis Framework

The TEF analysis framework (Burchard et al., 2018; Lorenz et al., 2019; MacCready, 2011) allows a consistent calculation of the transports and salinities of an exchange flow in salinity space. The main idea of TEF is that transports of volume and salinity in and out the estuary of the same salinity partially compensate since only the net exchange changes salinity and volume of the estuary. The transport of a tracer c using salinity coordinates S, $Q_S^c(S)$, through a cross section is defined as follows:

$$Q_S^c(S) = \left\langle \int_{A(S)} c\, u \, \mathrm{d}A \right\rangle, \tag{1}$$

where $A(S)$ denotes the area of a cross section with salinities greater than S, u is the velocity normal to the cross section (we define that positive values for u bring water into the estuary), and $\langle\ \rangle$ denotes temporal averaging. By differentiating $Q_S^c(S)$ with respect to S, one finds the exchange profile of tracer flux per salinity class:

$$q_S^c(S) = -\frac{\partial Q_S^c(S)}{\partial S}. \tag{2}$$

Lorenz et al. (2019) discussed in their paper two methods for computing the TEF bulk values, the *sign method*, which uses the positive and negative part of q_S^c (MacCready, 2011) and the *dividing salinity method*, which uses the extremum of Q_S^c as the salinity class, S_{div}, to separate the inflow and outflow (MacCready et al., 2018). The latter is used for this study and reads for an inverse estuary as

$$Q_{\mathrm{in}}^c = \int_{S_{\mathrm{min}}}^{S_{\mathrm{div}}} q_S^c \, \mathrm{d}S, \quad Q_{\mathrm{out}}^c = \int_{S_{\mathrm{div}}}^{S_{\mathrm{max}}} q_S^c \, \mathrm{d}S, \tag{3}$$

where S_{min} and S_{max} denote the minimum and maximum salinities of the used salinity space. The respective salinities are then calculated by the fraction of the salinity flux ($c = s$) and the volume flux ($c = 1$):

$$s_{\mathrm{in}} = \frac{Q_{\mathrm{in}}^s}{Q_{\mathrm{in}}}, \quad s_{\mathrm{out}} = \frac{Q_{\mathrm{out}}^s}{Q_{\mathrm{out}}}. \tag{4}$$

For most estuaries the density is mainly controlled by the salinity, which justifies the treatment in salinity space. But for the Persian Gulf, temperature gradients are not negligible and contribute to density gradients. Therefore, we will also investigate the exchange flow in potential density coordinates; that is, we replace S in (1)–(3) with the potential density ρ. For larger and especially deeper estuaries the exchange flow properties change with the season. This is also the case for the Persian Gulf where the bottom water in the Strait of Hormuz can be 10° colder than the surface waters (Reynolds, 1993), that is, summer water stratified over winter water. To study the seasonal exchange flow and the change of water masses, we take potential temperature Θ into account. We extend (1) by considering both salinity and potential temperature when computing the transports:

$$Q^c_{S,\Theta}(S,\Theta) = \left\langle \int_{A(S,\Theta)} c\, u \, \mathrm{d}A \right\rangle, \tag{5}$$

where $A(S,\Theta)$ now denotes the cross-sectional area with salinities greater than S and potential temperatures greater than Θ. Differentiation with respect to S and Θ allows the decomposition of the tracer flux in fluxes per salinity class and potential temperature class:

$$q^c_{S,\Theta}(S,\Theta) = -\frac{\partial^2 Q^c_{S,\Theta}(S,\Theta)}{\partial S\, \partial \Theta}, \tag{6}$$

which allows the analysis of the exchange flow in the form of a T-S diagram; see section 4.1. Equation (6) combines the TEF analysis framework with the T-S analysis framework used for the open ocean. Integration of (6) over all potential temperatures Θ yields (2), and the bulk values can be computed as described above:

$$q^c_S = \int_{\Theta_{\min}}^{\Theta_{\max}} q^c_{S,\Theta}\, \mathrm{d}\Theta. \tag{7}$$

Equivalently, by integrating over all salinities S (6) yields

$$q^c_\Theta(\Theta) = \int_{S_{\min}}^{S_{\max}} q^c_{S,\Theta}\, \mathrm{d}S = -\frac{\partial Q^c_\Theta(\Theta)}{\partial \Theta}, \tag{8}$$

which corresponds to the usual TEF using temperature instead of salinity as coordinates; see also Walin (1982). Using Q^c_Θ, one can similarly to (3) compute potential temperature fluxes, $\mathcal{Q}^\theta_{\mathrm{in,out}}$, and volume fluxes, $\mathcal{Q}_{\mathrm{in,out}}$, which then can be used to compute bulk potential temperatures:

$$\theta_{\mathrm{in}} = \frac{\mathcal{Q}^\theta_{\mathrm{in}}}{\mathcal{Q}_{\mathrm{in}}}, \quad \theta_{\mathrm{out}} = \frac{\mathcal{Q}^\theta_{\mathrm{out}}}{\mathcal{Q}_{\mathrm{out}}}, \tag{9}$$

where it should be noted that $\mathcal{Q}^\theta_{\mathrm{in,out}} \neq Q^\theta_{\mathrm{in,out}}$ and $\mathcal{Q}_{\mathrm{in,out}} \neq Q_{\mathrm{in,out}}$.

3. Model and Setup Description

The simulations in this study were performed with the General Estuarine Transport Model (GETM; Burchard & Bolding, 2002; Klingbeil & Burchard, 2013), which is a three-dimensional coastal ocean model (Klingbeil et al., 2018), solving the hydrostatic Boussinesq equations. Vertical turbulence is parameterized by an eddy-viscosity approach with k-ϵ closure in terms of stratification and shear (Burchard & Baumert, 1995; Rodi, 1987). For this the turbulence library from the General Ocean Turbulence Model (Burchard et al., 1999; Umlauf & Burchard, 2005) is linked to GETM. For lateral mixing we used the Smagorinsky (1963) parameterization with a Smagorinsky constant of 0.28 and a turbulent Prandtl number of 2 for tracers. The free surface is calculated by split-explicit mode splitting with drying-and-flooding capability (Burchard et al., 2004). For both the horizontal and vertical advection discretization, we used the Total Variation Diminishing-Superbee scheme (Pietrzak, 1998) to reduce the spurious numerical mixing of the transported quantities (Klingbeil et al., 2014)

The model setup, see Figure 1, uses a one nautical mile bathymetry based on ETOPO1 (Amante & Eakins, 2009), which is smoothed and adjusted to improve tide propagation. In the vertical 40 adaptive layers (Gräwe et al., 2015; Hofmeister et al., 2010, 2011) are used. The internal pressure gradient was discretized according to Shchepetkin and McWilliams (2003) to minimize errors due to the terrain-following coordinates. At 58°E

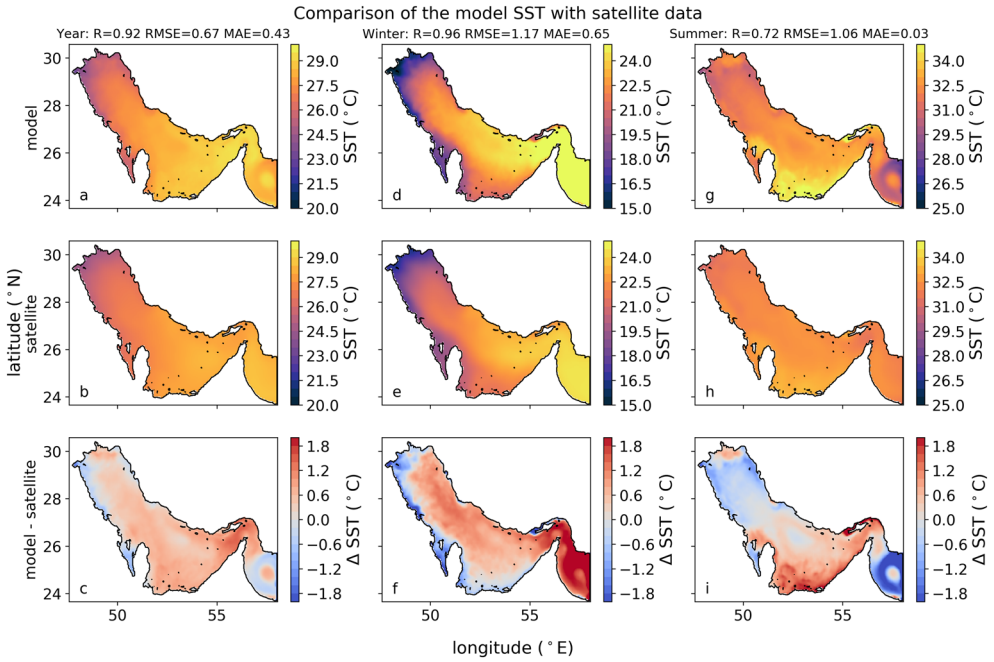

Figure 2. Comparison of the sea surface temperature of the model (a, d, and g) with OSTIA data (b, e, and h) (Stark et al., 2007) for the annual mean (a–c), winter (December, January, and February, d–f), and summer (June, July, and August, g–i) in 2015. Panels (c), (f), and (i) show the difference between model results and observations. In addition, the correlation *R*, the root-mean-square error (RMSE), and the mean absolute error (MAE) are provided for each column.

the open boundary is located, for which 3-hourly HYCOM data (Chassignet et al., 2007) with 1-hourly tide prescription by Oregon State University Tidal Prediction Software (OTPS, Egbert & Erofeeva, 2002) is used.

For meteorological forcing CFSR/CFS2 (Saha et al., 2010, 2011) is applied, using the Bignami bulk formula to compute longwave radiation (Bignami et al., 1995) and a Jerlov Type 1A water class (Jerlov, 1976), which suits the Gulf's water properties best (Al Azhar et al., 2016). The shortwave radiation is adjusted in a way that the mean value is reduced by 37 W/m^2 to account dust storms as Johns et al. (2003) described, based on Tragou et al. (1999). In addition, to account for the temporal change of the albedo due to the dust storms, we applied an additional cosine function with an amplitude of 20 W/m^2, which approximates the aerosol concentrations in the atmosphere quite well, as the greatest concentrations are found in June and July (Smirnov et al., 2002). The amplitude of 20 W/m^2 resulted in the least deviations in sea surface temperature (SST); see section 3.1.1. Rivers are prescribed by a constant value of 1,300 m^3/s for the Shatt Al Arab and by monthly climatologies from Kämpf and Sadrinasab (2006) for three other main rivers: Helleh, Mond, and Zohreh. To study the origin of the PGW, we marked the surface layer with different passive tracers in four areas: the shallow (< 30 m) south (Tracer 1, red), the northern shallow coast (Tracer 2, purple), the deeper (≥30 m) northeastern region (Tracer 3, blue), and the central and western part (Tracer 4, orange); see colored contours in Figure 1. For each baroclinic time step the tracers are passively transported and mixed. To guarantee that the sum of all tracers is less or equal to 1, the concentration of each tracer at the surface is reset to 0, except for the one in the specifically marked region, where it is set to 1. The model was initialized with temperature and salinity fields from HYCOM on 1 January 1993 and run until 1 January 2017. The spin-up time is 4 years, which is sufficient that the sum of all four tracers in each grid cell is 1.

3.1. Validation

3.1.1. SST

Comparison of the model's surface temperature with satellite measurements from the Operational Sea Surface Temperature and Sea Ice Analysis (Stark et al., 2007) is shown for 2015 in Figure 2 with computed correlation *R*, root-mean-square error, and mean absolute error (Willmott, 1981, 1982). The first row shows the model results for the annual mean, the winter season (December, January, and February), and summer season (June, July, and August). The second row shows the satellite SSTs and the third the difference between model and satellite. Comparing the annual distribution, the model is slightly warmer but agrees

Table 1
Dominant Tidal Constituents of the Persian Gulf

Station	M2	S2	K1	O1	N2	K2	P1
Bandar Abbas (mod)	92/195	35/228	34/7	20/7	22/176	10/222	11/5
Bandar Abbas (obs)	100/197	36/229	34/11	21/3	22/180	10/227	11/10
Bushehr (mod)	32/128	11/177	24/233	18/202	7/102	4/168	8/222
Bushehr (obs)	34/110	12/160	31/227	20/189	7/84	4/156	9/218
Shatt Al Arab (mod)	66/262	20/319	38/271	27/236	13/233	8/309	11/263
Shatt Al Arab (obs)	84/221	29/279	50/250	30/205	17/189	10/260	14/243
Ras Al Mishaab (mod)	13/328	3/28	29/281	21/245	3/276	1/22	9/269
Ras Al Mishaab (obs)	25/276	8/335	38/259	21/221	6/243	3/334	13/253
Jabal Fuwarait (mod)	23/42	7/73	16/72	9/32	6/14	2/74	5/65
Jabal Fuwarait (obs)	42/44	13/88	20/54	9/0	11/17	4/88	7/54
H. al Mubarras (mod)	24/287	10/342	30/119	19/80	5/265	4/330	9/109
H. al Mubarras (obs)	28/261	13/315	43/102	23/52	4/232	3/315	14/102
Dubai (mod)	37/248	12/286	14/106	13/69	8/223	4/279	5/91
Dubai (obs)	44/237	16/281	23/91	16/42	10/217	5/265	7/77

Note. The results are computed for the Year 2014 and are shown with amplitude (cm)/phase shift (°) compared to Greenwich for several stations in the Gulf; see Figure 1 for the locations. Observational data are taken from Pous et al. (2012) (Tables 1 and S2).

well with the observations ($R = 0.92$). The winter season shows colder northern and eastern coasts and warmer temperatures toward the Strait of Hormuz. The model and the observations show the same temperature distribution ($R = 0.96$) with the model being colder at the coasts and warmer in the deeper regions, especially in the Gulf of Oman near the open boundary. In summer, the model shows a very warm southern coast, which is deviating from the observations by up to 2 °C ($R = 0.72$). Again, the temperature distribution near the open boundary is up to 2 °C colder than the observations.

A comparison for all years is provided in Table 1 for SST products of National Oceanic and Atmospheric Administration Optimum Interpolation SST (Reynolds et al., 2007) and Operational Sea Surface Temperature and Sea Ice Analysis (Stark et al., 2007) in the supporting information of this publication. All simulation years show the described discrepancies in varying strengths, that is, colder coasts in winter and a warm southern coast, and being in general slightly warmer than the observations.

3.1.2. Heat and Fresh Water Fluxes

Heat and fresh water fluxes are besides wind the main drivers of the dynamics in the Gulf. Figure 3 shows the climatological annual cycle of the model simulation. The mean net heat flux of $-4.7\,W/m^2$ ($-8.3\,W/m^2$ for 1997) is in the range of other studies: -7 ± 4 to $4\,W/m^2$ (1997) (Johns et al., 2003), $-4\,W/m^2$ (Kämpf & Sadrinasab, 2006), $-3\,W/m^2$ (Thoppil & Hogan, 2010), and -7 to $-10.3\,W/m^2$ (Yao & Johns, 2010a). Precipitation $P = 0.11$ m/a and evaporation $E = 1.62$ m/a agree with other studies as well: $P = 0.15$ m/a, $E = 1.58$ m/a (Johns et al., 2003), $P = 0.21$ to 0.24 m/a, $E = 1.51$ to 1.61 m/a (Pous et al., 2015), and $E = 1.8$ m/a (Kämpf & Sadrinasab, 2006). The seasonal cycle of the heat fluxes and net fresh water flux is in agreement with previous studies (Yao & Johns, 2010a). The net fresh water fluxes show higher evaporation rates in fall than in spring. The error bars denote the standard deviation of the monthly means of the 24 simulation years. The greatest variations can be found for the evaporation rate, which transfers to the latent heat flux. The other heat fluxes show little annual variations. Since the incoming shortwave radiation, its distribution and strength is a major uncertainty in the Gulf region; we provide the model's calculated annual mean surface fluxes for heat and fresh water in Table S2 in the supporting information of this publication.

3.1.3. Tides

The Gulf experiences strong mixing due to tides especially in the Strait of Hormuz (Alosairi et al., 2011), and therefore, the model shall reproduce the tidal gauges. A harmonic analysis for the main tidal components was carried out and the results for the amplitude (cm) and phase (°) compared to Greenwich are listed in Table 1. Overall, the tidal wave is slightly faster and the amplitudes are slightly smaller than the observations

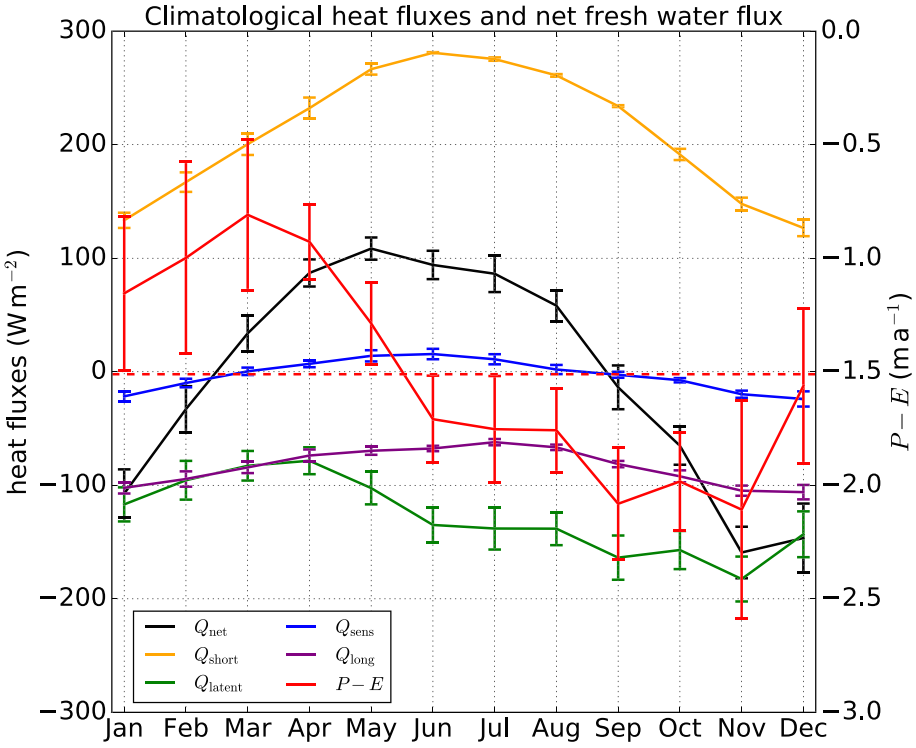

Figure 3. Climatological surface heat fluxes and fresh water fluxes (1993-2016): net heat flux Q_{net} (black), shortwave radiation Q_{short} (orange), latent heat flux Q_{heat} (green), sensible heat flux Q_{sens} (blue), longwave heat flux Q_{long} (purple), and the net surface fresh water flux as the difference of precipitation P and evaporation E, $P-E$, (red). Positive value denote a flux into the Gulf. The error bars denote the standard deviation to indicate the natural interannual variability.

show. Nevertheless, for the area of main interest, the Strait of Hormuz, the tidal components are correct (Bandar Abbas).

3.1.4. Salinity and Potential Temperature Distribution Along the Gulf Axis

The structure along the Gulf axis, TR_1, for potential temperature and salinity shows two completely different states: a well-mixed state in winter (January) and a well-stratified state in summer (July); see Figure 4. Similar depictions can be found in Reynolds (1993) or Yao and Johns (2010b) for measurements of the Mt. Mitchell expedition or in Swift and Bower (2003) for climatological distributions, as well as for model studies, for example, Yao and Johns (2010b). The along-axis structures of this study compare well to the

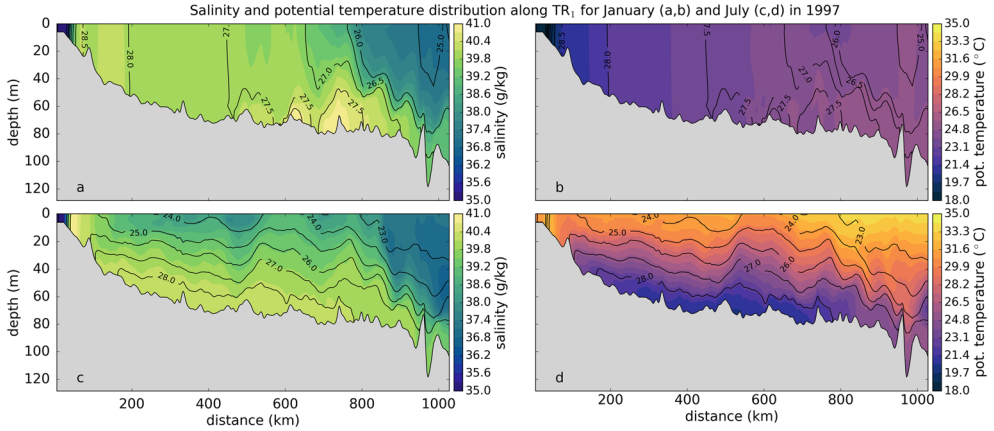

Figure 4. Model results of the mean salinity, mean potential temperature, and mean potential density anomaly (contour lines) distribution along the Gulf axis TR_1 for January (a, b) and July (c, d) 1997.

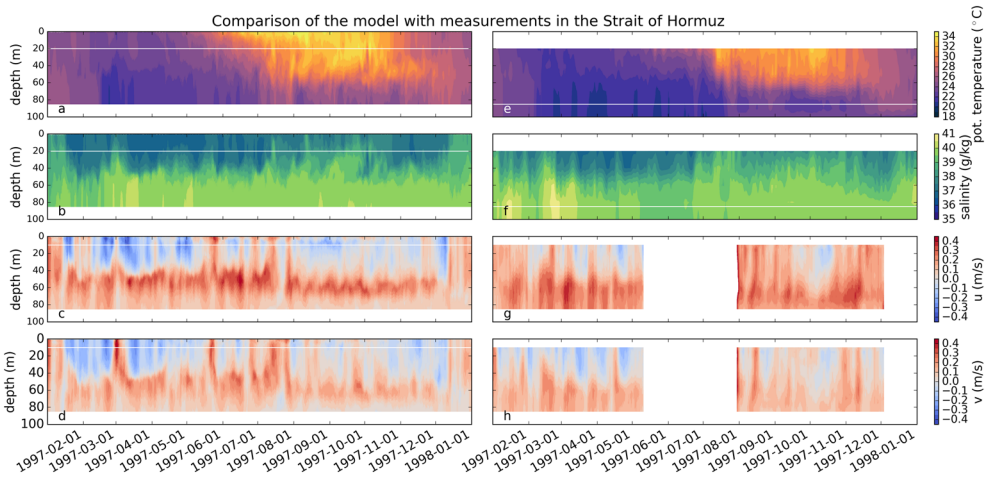

Figure 5. Comparison of model results (a–d) for potential temperature, salinity and zonal (u) and meridional (v) velocities in the Strait of Hormuz; see red dot in Figure 1, with measurements from Johns et al. (2003). (e–h) Both, the model data and the observations, were smoothed using a running mean of 24-hr width.

observations. In winter the Gulf is well mixed, that is, homogeneous water columns, with high salinities and cold potential temperatures in the northwest. Toward the Strait of Hormuz there is stratification occurring with IOSW stratifying over PGW due to the exchange flow. In summer the whole Gulf is vertically stably stratified with increasing salinity at the surface toward the northwest. In addition, the doming of the isolines shows the signature of the large cyclonic eddies of the Gulf wide circulation (Thoppil & Hogan, 2010).

3.1.5. Strait of Hormuz

We showed that the general structure of the Gulf is well represented in the model. Now we compare the model temporal evolution in the Strait of Hormuz to measurements of Johns et al. (2003) for potential temperature, salinity, and velocity components; see Figure 5. The data were smoothed, using a 24-hr running mean. Comparing Figures 5a and 5e, the temporal evolution of potential temperature agrees in terms of timing and depth of the thermocline. The cold winter water in the observations from mid-February to July is warmer in the model. Similarly, the summer potential temperatures above the thermocline are warmer. Comparing the salinity evolution in Figures 5b and 5f, the salinities match the observations in two important characteristics: first, the uplift of the halocline due to propagating eddies (Thoppil & Hogan, 2009) and second, the general uplift of the halocline from July to November, although the second is not as pronounced in the model as in the observations. In the supporting information of this publication we show time series for potential temperature and salinity at four depths, which show the agreements and the deviations in more detail. Comparing the velocity components u (zonal) and v (meridional), a general northeastward current is persistent below 40 m in both model and observations. Maximum velocities are found between 40 and 60 m in the model and 50–70 m in the observations. Propagating eddies are existent over the whole year in the model and in the first half of the observations.

4. Results

4.1. TEF Diagram

The extended TEF analysis as described in section 2.1 of the climatological results along TR_{11} in June is shown in Figure 6. The structure of the diagram is inspired by Döös and Webb (1994) who showed in a similar structure the volume transport depending on depth and density. The lower left panel shows $q_{S,\Theta}$ with the dashed line denoting the potential density, the upper panel shows q_S, and the right panel shows q_Θ. The dashed lines in the last two panels denote the dividing salinities/potential temperatures, separating inflow and outflow (Lorenz et al., 2019), the gray shade shows the standard deviation, and the red and blue dot the respective representative bulk value of salinity or potential temperature of the inflow and outflow.

$q_{S,\Theta}$ shows two distinct water masses. In red the inflowing IOSW with salinities of ~37 g/kg and a wide range of potential temperatures, 25–35 °C, and in blue the outflow of PGW with higher salinities and colder

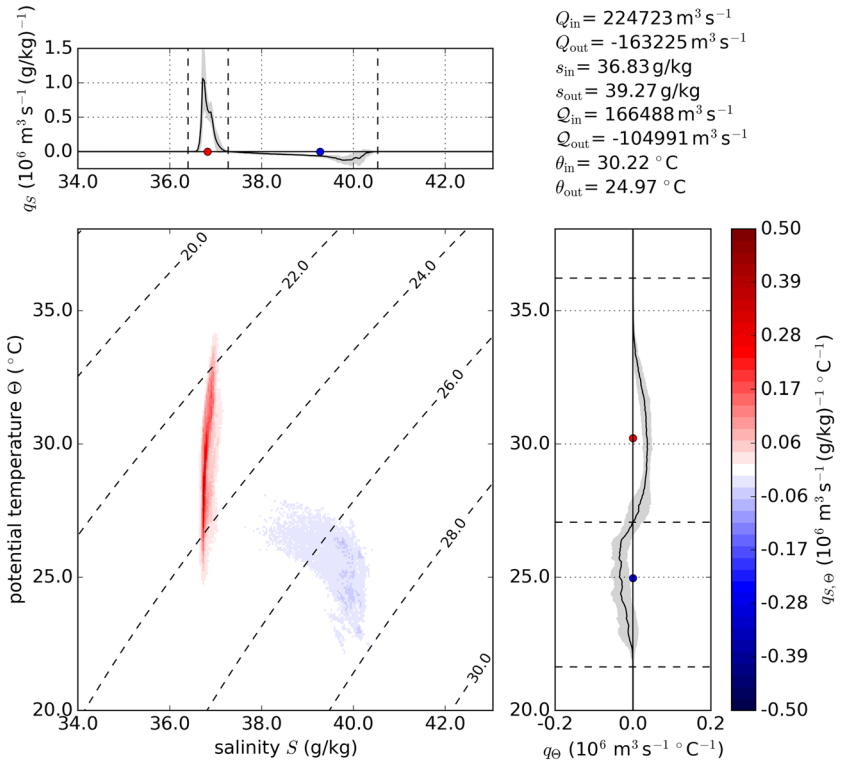

Figure 6. TEF diagram and TEF profiles in salinity and potential temperature space for the climatological results of TR_{11} in June. The main panel shows the color coded volume transport per salinity and potential temperature class $q_{S,\Theta}$. By integration along one of the axis of $q_{S,\Theta}$ two different TEF profiles are found with different volume fluxes for inflow and outflow: classic TEF profile in salinity coordinates (top panel) and TEF profile in potential temperature coordinates (right panel). In addition, the computed bulk values of the exchange flow are listed in the top right. The depiction structure is inspired by Döös and Webb (1994).

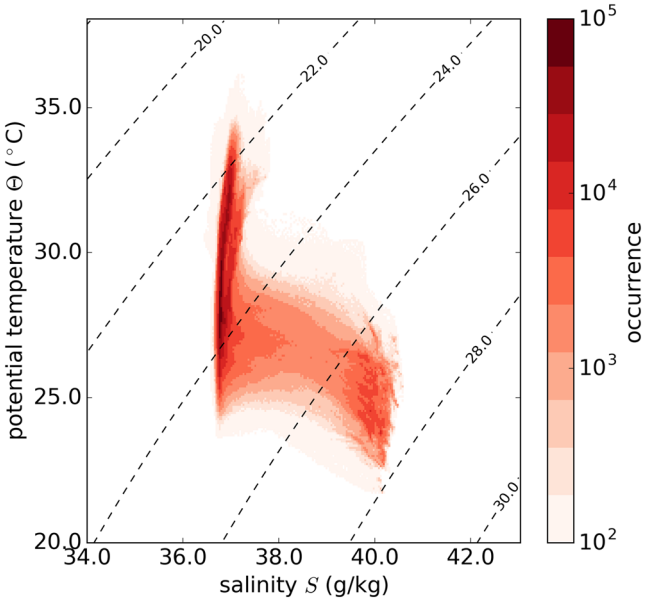

Figure 7. Conventional T-S diagram of the data behind the TEF diagram (Figure 6). Color depicts the occurrence of the potential temperature-salinity combination.

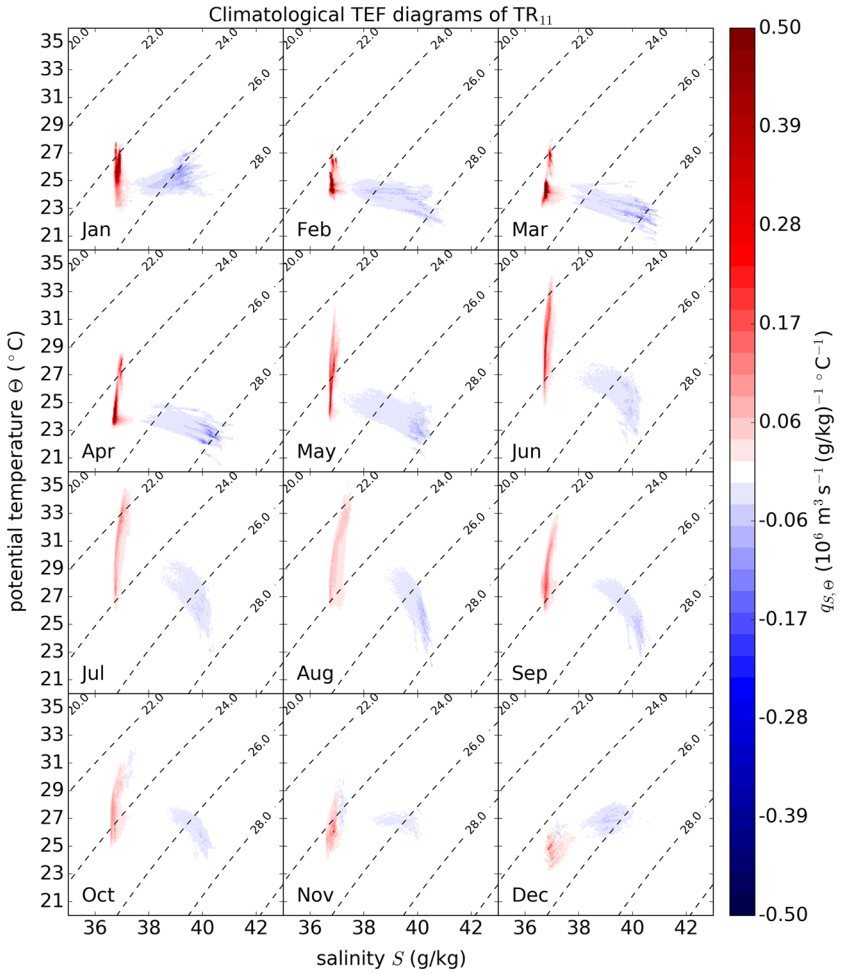

Figure 8. Climatological TEF diagrams for the analysis period from 1997–2016 along TR_{11}. Each panel shows the climatological results for one month with color coded volume transport per salinity and potential temperature class.

potential temperatures. The general wider spread of salinities and potential temperatures of the PGW indicates the entrainment process where both water masses are mixed. In contrast to this depiction, Figure 7 shows a conventional T-S diagram of the same data used for Figure 6, where color denotes the occurrence of the potential temperature-salinity combination. The occurrence value is weighted with the layer height, which is variable in time and space in the used model. Comparing both figures, one finds that many potential temperature-salinity combinations do not contribute to the exchange flow in terms of TEF. Especially, the mixture of both water masses and values that only rarely occur does not contribute. This could have two reasons: First, the transports for these combinations are very small, and second, the transport partially compensates each other, meaning positive and negative transport add up with no significant transport being left in the Θ-S combination. On the other hand, the cores of the inflow and outflow in the TEF diagram correspond to high numbers of occurrence.

Integration along Θ in Figure 6 yields to the classical TEF profile in salinity space (upper panel), which is then used to compute the bulk values Q_{in}, Q_{out}, s_{in}, and s_{out} using the dividing salinity method (Lorenz et al., 2019). The profile shows a clear signature of the IOSW as distinct positive values in salinity classes around 37 g/kg and the PGW as a less pronounced peak around 40 g/kg. The outflow from ~37.5 to ~39.5 g/kg is a mixture of both water masses due to entrainment as mentioned before. Integration along S yields a TEF profile in potential temperature space (right panel). The resulting profile shows one inflow and outflow as well, but while in salinity space inflow and outflow are clearly separated, there is additional compensation in potential temperature from ~25–28 °C. This compensation causes that $Q_{in} \neq \mathcal{Q}_{in}$ and $Q_{out} \neq \mathcal{Q}_{out}$. This result motivates that the representative potential temperatures must be computed in potential temperature space,

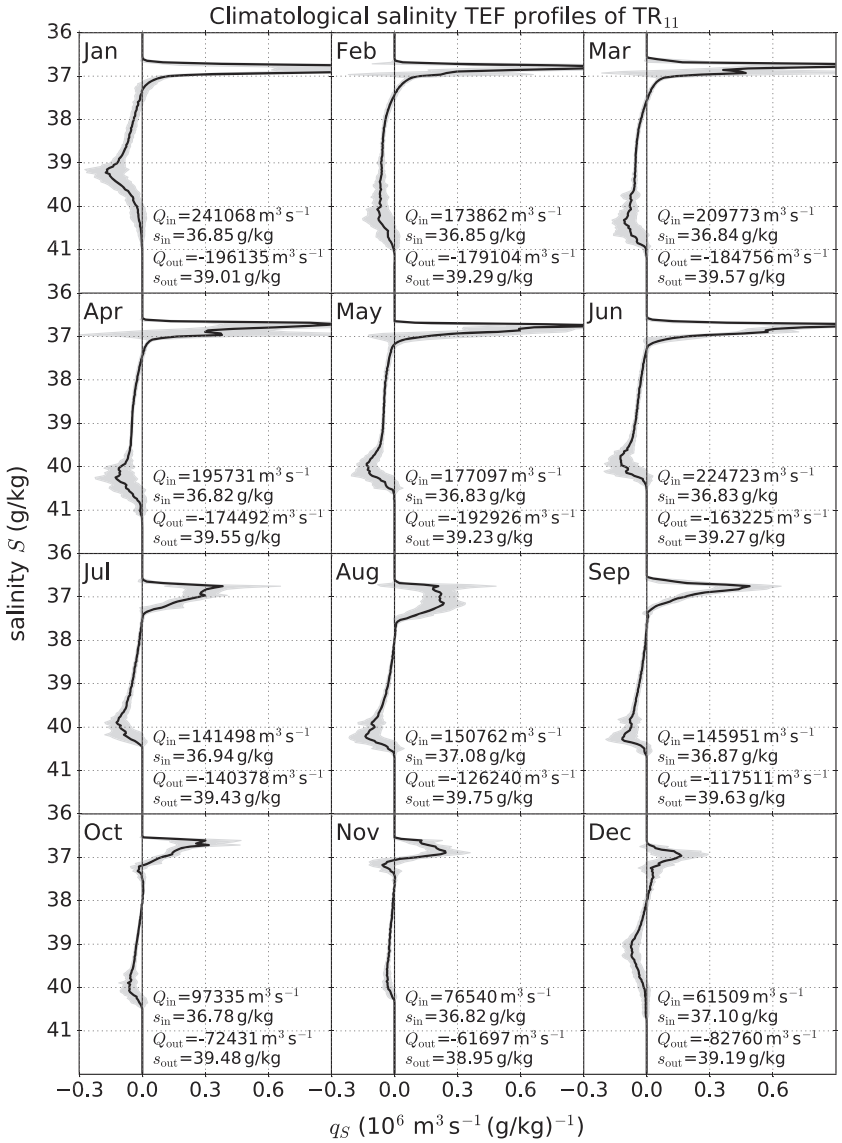

Figure 9. Climatological TEF analysis for the analysis period from 1997–2016 along TR_{11} in salinity coordinates. For each month, the bulk values for volume transport and representative salinities are computed with $N = 2^{16}$ salinity bins.

because the heat flux in salinity space would not include the compensation and therefore overestimates the heat exchange.

Integration along isopycnals ρ will lead to an exchange profile in potential density coordinates. This will lead to additional values of volume transport, probably being different than the other two transport pairs. Yet this approach will find the correct representative bulk values for potential density. We elaborate more on this in the next section.

4.2. Climatological Exchange Flow

To analyze the seasonal exchange flow of the Gulf, we employ TEF diagrams for the monthly climatology in Figure 8. The diagrams show a distinct separation of the inflow (red) and outflow (blue) throughout the year. The inflow covers a narrow salinity range around 37 g/kg and dependent on the season a wider range in potential temperature for all months. Highest potential temperatures of the inflow are found in July and August, lowest in December. The outflow on the other hand covers a wider salinity and potential temperature range with changing properties in different seasons. First, the potential temperature of the outflow is overall colder than the inflow with December being the exception where the potential temperature of the

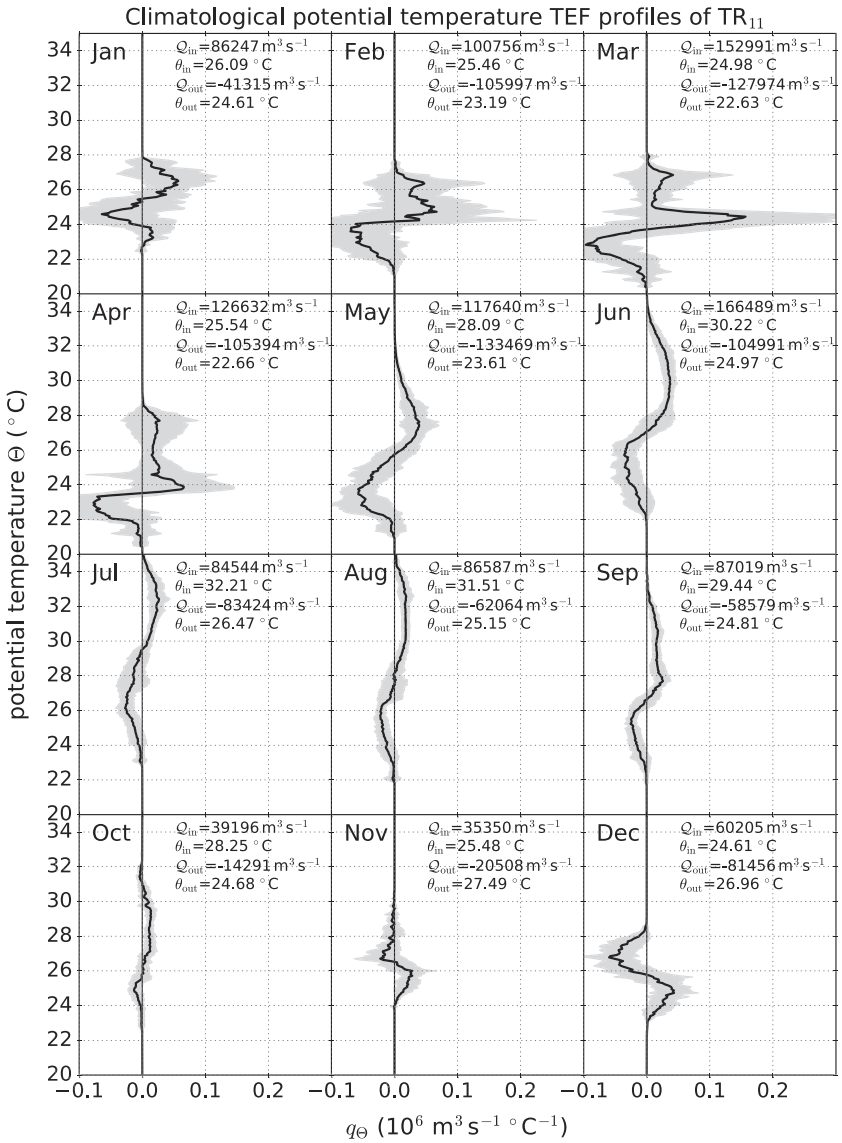

Figure 10. Climatological TEF analysis for the analysis period from 1997–2016 along TR_{11} in potential temperature coordinates. For each month, the bulk values for volume transport and representative potential temperatures are computed with $N = 2^{16}$ potential temperature bins.

inflow is colder. From January to March the potential temperatures are comparable, from April to September the potential temperatures are colder and in October and November the potential temperatures are again comparable. Whereas from December to May the transition from inflow to outflow seems continuous along the salinity axis, there is a salinity gap from June to November of more than 1 g/kg. Interestingly, in October, November, and December outflowing water can be found at high temperatures and salinities in the range of 37–37.5 g/kg. To follow the classical TEF analysis framework and to give more detailed insights into the salinity distribution, Figure 9 shows the TEF profile for q_S (black line) in salinity space, including the standard deviation (gray contour) and the respective TEF bulk values. Taking a closer look onto the shape of the profiles one recognizes the distinct peak for the inflow, which is highly variable from February to May. From July to December the salinity range widens. The bulk values show that the inflow is stronger during the first half of the year. The bulk salinity s_{in} is not changing much. The transition zone, which we mentioned before, shows one sharp crossing of the zero line from January to May, but q_S is very close to the zero line for ~1 g/kg before becoming clearly negative for the other months. This results in the gap between inflow and outflow one sees in Figure 8. The outflow extends over a broad salinity range from 37.5 to ~41 g/kg. The shape and the location of the maximum outflow per salinity class (minimum of q_S) vary over the season.

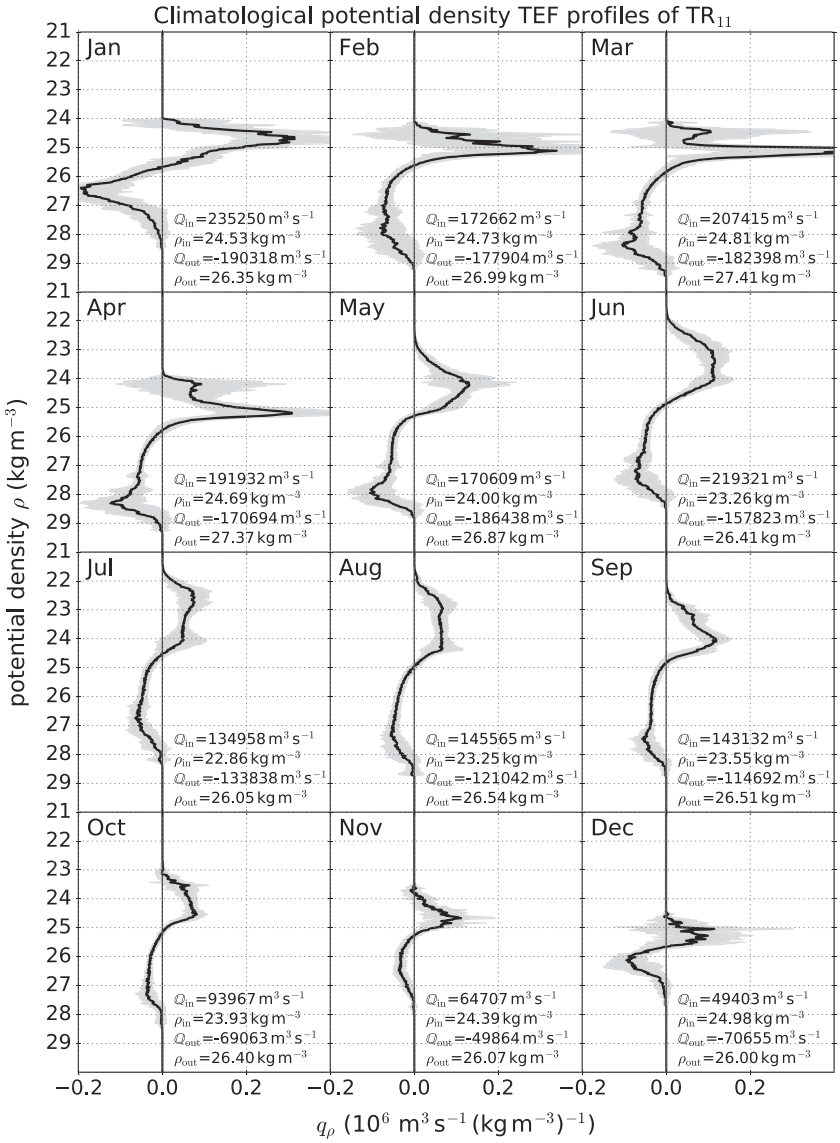

Figure 11. Climatological TEF analysis for the analysis period from 1997–2016 along TR_{11} in potential density coordinates. For each month, the bulk values for volume transport and representative potential densities are computed with $N = 2^{16}$ potential densities bins.

The maximum is shifting from salinities around ~39 g/kg in December and January toward higher salinities between ~40 and 41 g/kg in March and April, then decreasing again toward lower salinities < 40 g/kg in June before increasing again in August and September, and finally decreasing toward the starting situation in December. s_{out} follows this seasonal dependency. Highest salinities are found in March and April with salinities > 41 g/kg, but highest s_{out} is found in August. In October and November one sees the signature of an outflow at salinities around 37.5 g/kg, which was seen before in the TEF diagrams. Similarly to the inflow, the bulk values of the outflow show stronger transport in the first half of the year, and weaker transport in the second half with the lowest transport in November and strongest in January.

Similarly to Figure 9, Figure 10 shows the climatological potential temperature TEF profiles with the respective bulk values. The TEF potential temperature profiles show as the TEF salinity profiles a two-layered exchange flow (with the exception of January, but the shapes of the profiles change considerably over the year). The January profile shows a three-layered exchange flow. The bulk values in Figure 10 are the correct bulk values, which treat the two inflow layers as one. Separating the inflow into the two layers yields $\mathcal{Q}_{in,1} = 11,892\,m^3/s$, $\mathcal{Q}_{in,2} = 74,240\,m^3/s$, $\theta_{in,1} = 23.45\,°C$, and $\theta_{in,2} = 26.52\,°C$. All profiles show an inflow

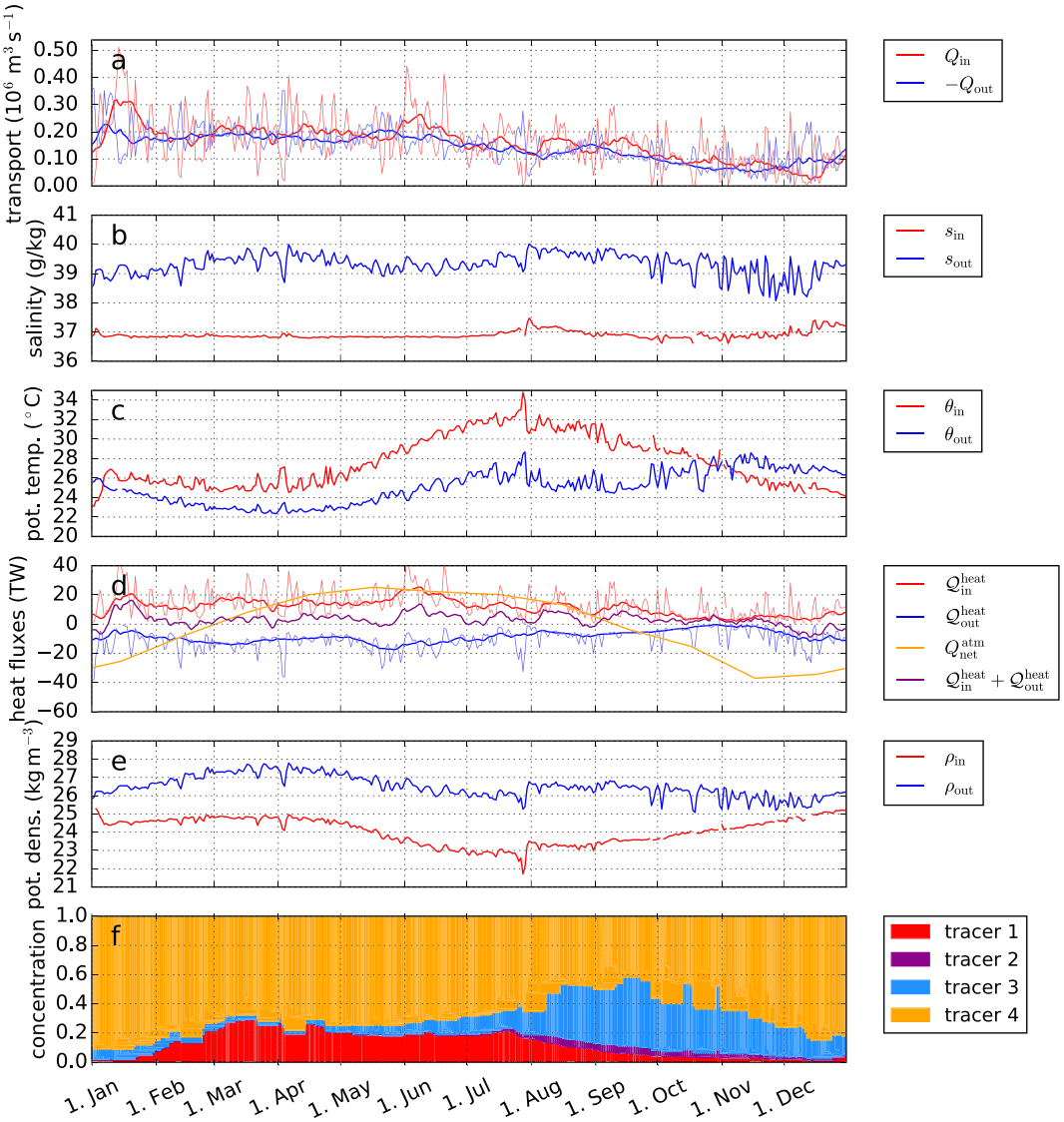

Figure 12. Time series of climatological daily TEF bulk values along TR_{11}: in (a) the transport (thick lines: 14-day running mean, thin lines: daily values), in (b) the bulk salinities, in (c) bulk potential temperatures, (d) heat exchange (thick lines: 14-day running mean, thin lines: daily values) and surface heat fluxes (monthly mean) (e) the bulk potential densities, and in (f) the tracer concentrations of the outflow. Blank spaces indicate that for that climatological day there was no two-layer exchange.

of warmer water and an outflow of colder water, except November and December where the situation is reversed. From January the potential temperatures of the inflow increases until July and the outflow potential temperature decreases until April, where the coldest potential temperatures are found as well. Warmest potential temperatures are found in July and August. From August the inflowing potential temperature decreases until the the end of the year. The outflowing potential temperature is warmest in November and December. θ_{out} follows the cycle of s_{out} but inversed. When s_{out} shows the higher values, θ_{out} shows smaller values. This link of the properties of the outflow indicates a change in the origin of the water, which will be further investigated in the following section 4.3. The values for the volume transport also indicate a stronger exchange flow in the first half of the year.

Since density is the dynamical relevant quantity, we also integrated along isopycnals in the TEF diagram yielding potential density TEF profiles in Figure 11. The density TEF results show the seasonality as well as the change of the origin of the outflow in August/September. For these months the outflow's density bulk value increases. The volume flux bulk values are very close to the ones of salinity TEF with the exception of

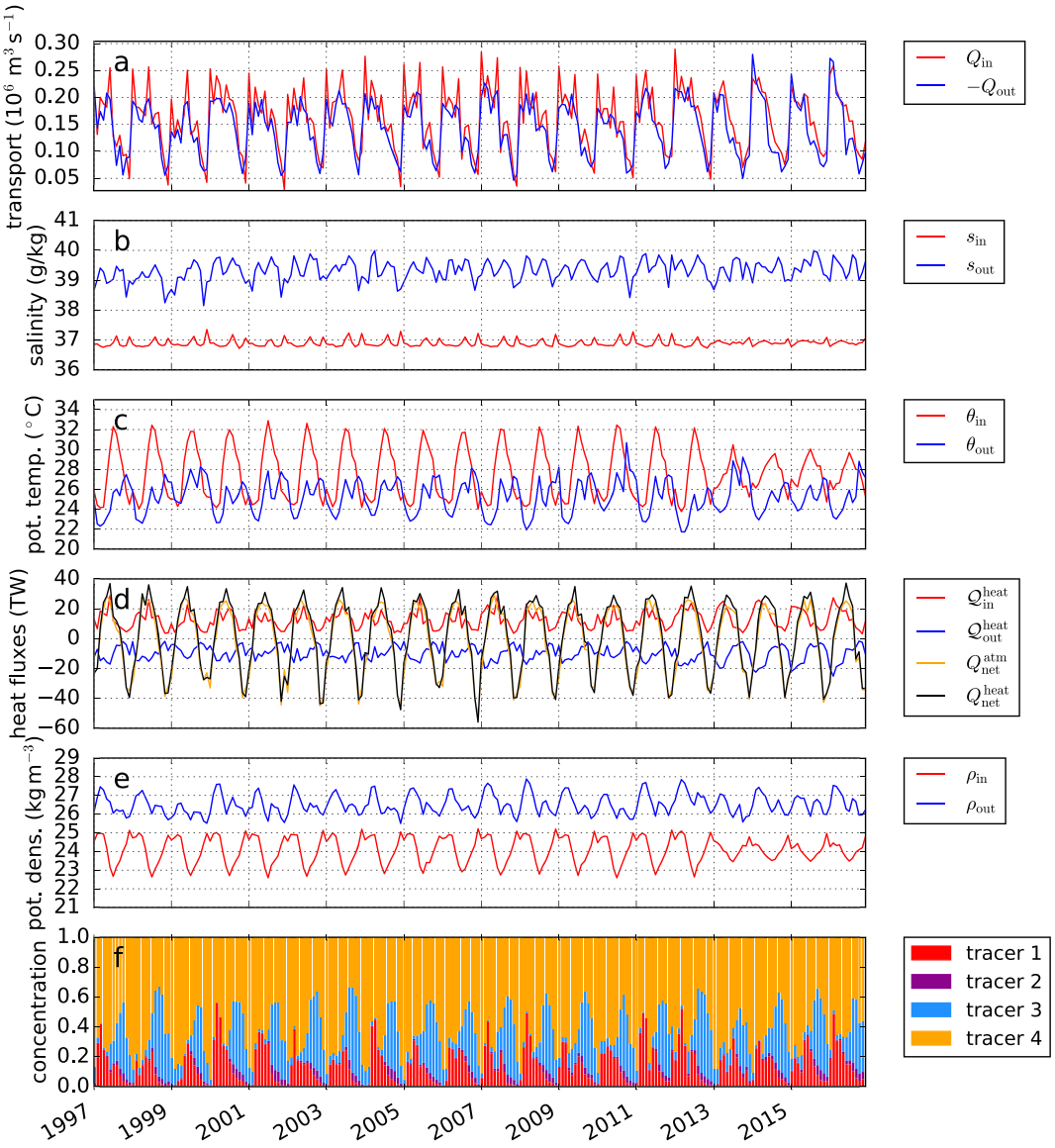

Figure 13. Time series of monthly TEF bulk values along TR_{11}: in (a) the transport, in (b) the bulk salinities, in (c) bulk potential temperatures, in (d) heat exchange and surface heat fluxes ($Q_{net}^{heat} = Q_{in}^{heat} + Q_{out}^{heat} + Q_{net}^{atm}$), in (e) the bulk potential densities, and in (f) the tracer concentrations of the outflow.

November and December as the inflow and outflow are well separated in salinity and density coordinates for these months. In November and December, there is additional compensation in density coordinates, decreasing the volume exchange bulk values.

4.3. Time Series of the Exchange Flow

We have seen the climatological exchange flow and its salinity, potential temperature, and potential density distribution. In this section we take a closer look into the temporal evolution of the computed bulk values, the heat budget, and the composition of the outflow using the tracers we introduced in section 3. Figure 12 shows the climatological daily bulk values of the transport in (a), the salinities in (b), the potential temperatures in (c), the heat exchange in (d), the bulk potential densities in (e), and the tracer concentrations of the outflow in (f). It should be noted that the time series only shows one bulk value for one inflow and outflow or a blank if there was none on that climatological day. Multiple inflows or multiple outflows, like in January in Figure 10, were combined to one value by weighted averaging (Lorenz et al., 2019). All time series show a very high variability, especially for the volume transport. The climatological results from section 4.2 showed

that s_{out} and the maximum salinities changed with the seasons and had two peaks: one in March/April and a second in August/September. The time series of s_{out} in Figure 12b shows these changes as well. Similar changes can be found in the potential temperatures of the outflow in Figure 12c where the potential temperature drops when the salinity increases. ρ_{out} in Figure 12e shows an increase at the same times. This variability can be explained with the composition of the outflow in Figure 12f. It shows the respective outflow bulk values, that is, fraction of water origin with values between 0 and 1, for the different tracers $c_{i,out}$ using the salinity coordinates as these represent the PGW properties. The sum of the tracers in each grid cell after the spin-up time is 1, meaning we can exactly decompose where the water was last in contact with the atmosphere. In orange, the eastern surface waters were marked which for the outflow can be interpreted as the fraction of entrained water. January, which showed the strongest exchange, shows the highest fraction of entrained water. For February to July most of the water, despite the entrained water, comes from the southern shallows (red), while from August to December most water comes from the deeper (<30 m) northern parts (blue) and only a small amount (<10%) comes from the northern shallows (purple). This regime shift from water of the southern shallows to water from the north explains the water property change in s_{out}, θ_{out}, and ρ_{out}. Before this shift there is a rapid increase of ~2 °C in θ_{in} and therefore a decrease in ρ_{in}. This coincides with a very small volume inflow at the surface. During the shift, the inflow properties show a short small increase in salinity and density, showing that for a short period the inflow consisted of a mixture of both water masses. Figure 12d shows the bulk values for heat c=$\theta\rho$cs, $Q^{heat}_{in,out}$ (ρ: potential density and c_s: specific heat capacity of water), the net surface heat flux Q^{atm}_{net}, and the net heat exchange with the Indian Ocean as the sum of $Q^{heat}_{in,out}$. The net heat transport through the transect is always positive, that is, importing heat into the Gulf, except in December, where heat is exported. This net heat import is highly variable on short timescales but on average replacing the net heat loss into the atmosphere; see also section 3.1.2. To study potential trends and interannual changes during the simulation period we computed monthly bulk values for each year; see Figure 13. The monthly bulk values for transport, salinity, potential temperature, potential density, and heat show similar annual cycles for each year until 2012. From there on the bulk values differ significantly from the years before, especially for the potential temperature the bulk values for θ_{in} are suddenly 2° colder. The reason for this is found in the change of the boundary data. From 2012 the HYCOM simulation changed and therefore the boundary data we apply. The data change from 3-hourly to daily values changes the inflow properties significantly, and the outflow properties insignificantly; see also section 5.2.

5. Discussion

5.1. TEF Diagram

The TEF diagram extends the presentation of the exchange flow by including potential temperature as a second coordinate. This allows gaining insight into the potential temperature-salinity structure, which provides a better understanding of the exchange flow and distinctions between different contributing water masses. Similar frameworks have been applied to study the water mass transformation and overturning circulation, that is, for the Atlantic Ocean (Döös et al., 2012; Groeskamp et al., 2019; Hieronymus et al., 2014; Speer, 1993; Worthington, 1981; Zika et al., 2013). In addition, it can be easily compared to other T-S diagrams with the restriction that the TEF diagram is a subset of a classical T-S diagram due to the partial compensation. Yet because of this reason, the TEF diagram reduces and simplifies the conventional T-S diagram to the relevant potential temperature-salinity combination, which contribute to the exchange flow. The two coordinates presented in this framework could be easily exchanged to other coordinate combinations, that is, potential density (driving the physics) and one being important for the biogeochemistry, for example, oxygen (Groeskamp et al., 2019).

The exchange flow in salinity and potential temperature coordinates yields T-S diagrams with color-coded transport per salinity and potential temperature class. By integration along either of the axis, one finds the classical TEF profile for the other. From these one can compute the bulk values via the dividing salinity method (Lorenz et al., 2019). The results from section 4.1 show that the TEF profiles for potential temperature and salinity do not provide the same bulk values for volume exchange. The reason is found in different compensation when sorting the respective fluxes into salinity or potential temperature bins. This opens the question which coordinate system should be used to compute the bulk values. For quantifying the exchange flow of an arbitrary tracer c we think that one should compute the respective bulk values using the tracer as coordinates. For the estuary only the net exchange is important and therefore the tracer flux per tracer

class, that is, salinity space for salinity bulk values and potential temperature space for potential temperature bulk values.

Because of the different compensation in different coordinates, the TEF bulk values are not necessarily representative for the water bodies but definitely representative for the exchange flow. To be representative for the water bodies, one would have to compute the bulk values from the two-dimensional $q_{S,\Theta}$ or $Q_{S,\Theta}$. For example, instead of finding one dividing salinity, one would have to find one line that separates the inflow and outflow, which aggravate the automatic computation of the volume fluxes. Especially for multilayer exchange flows, the inflows and outflows may not be as clearly separated as for the Persian Gulf.

5.2. Exchange Flow of the Gulf

The results show a seasonality of the exchange flow with stronger exchange flow in terms of transport in the first half of the year and a weaker exchange flow in the second half. The corresponding inflowing properties are a relatively stable value for salinity of $s_{\text{in}} \approx 37$ g/kg and a seasonal potential temperature, and therefore heat, which follows the seasonal cycle of solar radiation. The outflowing properties are dependent on the origin of the water and the amount of entrained water. For the first half of the year, most of the water originated at the southern shallows, which is entrained on its path toward the Strait of Hormuz. In the middle of the year, the waters origin changes from south to north with only a minor contribution of the northern shallows. This change of water masses changes the bulk salinity and potential temperature of the outflow toward higher salinities, colder potential temperatures, and therefore higher potential density. The heat budget is dominated by the surface heat fluxes, yet there is a net heat import through the Strait of Hormuz, which compensates for the net surface heat loss.

The computed transport of the outflow can be compared to the values of other studies with reservation since the TEF bulk values are different from the Eulerian transports (Burchard et al., 2018; MacCready, 2011). But the seasonality and different strength compares well to the results of Yao and Johns (2010b). Compared to the results of Pous et al. (2015), the seasonality compares, but the transports are generally higher in their study. The shape of the climatological TEF diagrams compares well to the T-S diagram provided in Kämpf and Sadrinasab (2006) with data from Alessi et al. (1999) and Pous et al. (2015). However, the maximum salinities in Pous et al. (2015) are less than the values in this study or the observation from Alessi et al. (1999) for the Strait of Hormuz.

We conclude from these results that the seasonal formation of PGW can be described as follows: In fall, when the evaporation rate is highest and the net surface heat flux becomes negative, the stratification of the Gulf vanishes due to buoyancy loss and leads to dense and hypersaline, cold water, especially in the shallow regions in the north and south. The water is well mixed in late fall/early winter; see Figure 4, and horizontal density gradients are formed, which create a bottom gravity current toward the Strait of Hormuz. When vertical mixing becomes weaker in late winter and spring, the exchange flow strengthens comparable to the removal of a lock in a lock exchange. The dense water from the southern shallows arrives in the Strait of Hormuz in winter until the end of spring, which was also found by Kämpf and Sadrinasab (2006). In summer the first water of the north arrives in the Strait and slowly replaces the water from the south, which has become to warm and thus too light. The southern water formed in spring becomes part of the surface recirculation (Yao & Johns, 2010b) during this time. In August/September most of the outflowing water originates from the north, creating the second peaks in s_{out}, θ_{out}, and ρ_{out}. The tracers suggest that most of the dense northern water is not formed in the shallow, but the deeper area (depth greater than 30 m) due to the well-mixed state of the Gulf and the greater volume. Although the water in the deeper northern part may not be as dense as the water from the northern shallows, the water is mixed down and becomes part of the bottom current. This formation is in agreement with Yao and Johns (2010b).

Despite the change in boundary forcing, which changed the bulk values, especially for the inflow θ_{in} and therefore also ρ_{in}, the exchange flows varies from year to year; see Figure 13 as well as the standard deviation in Figures 9 and 10. These can be related to interannual changes in the atmospheric forcing as the boundary potential temperatures and salinities in the upper layer of the boundaries do not show any significant variability except a seasonal cycle. Especially, the wind fields and potential temperatures play an important role for the evaporation, which is the major driver of the exchange flow. As the exchange flow varies annually we do not find any signal of timescales greater than 1 year in the bulk values. The internal interannual variability in the atmospheric forcing is of greater importance for the variability of the exchange

flow than the bias in the boundary conditions. Even though the boundary conditions changed, the transformation of IOSW to PGW is robust in the simulation as the outflow properties are within the variability of the years before. Nevertheless, for future long-term studies consistent data sets to force the model would be of great benefit.

6. Summary and Conclusions

This study investigated the potential temperature-salinity structure of the exchange flow of the Gulf by applying the TEF analysis framework (MacCready, 2011) to the results of a 24-year high-resolution simulation using GETM. The TEF analysis framework was extended to include a second coordinate, potential temperature in this case, which leads to a TEF diagram instead of profiles. This two-dimensional decomposition of the exchange flow gives a more detailed insight on the composition of the exchange flow. The model reproduces the general overturning circulation of the Gulf, and the results are in agreement with other studies. We could show that the evolution of the exchange flow follows a seasonal cycle with stronger exchange in spring and summer, than in fall and early winter, that is, Yao and Johns (2010b) and Pous et al. (2015). This is also true for the potential temperature-salinity distribution of the water in the Strait of Hormuz, that is, Alessi et al. (1999). In addition to the volume transport, we provide bulk values for the salinity and potential temperature for the inflow and outflow, which completes the description of the exchange flow. The potential temperature coordinates allowed the computation of the heat exchange through the analyzed transect. Furthermore, the TEF profiles and TEF bulk values for s_{out}, θ_{out}, and ρ_{out} showed a change to higher salinities, lower potential temperatures, and therefore higher potential densities in August/September. We showed with a tracer experiment that this change is associated to a shift of the origin of the PGW. While in winter and spring the PGW originated in the southern shallows, in summer between August/September most water originated from the northern part of the Gulf. This finding underlines the benefits of the two-dimensional TEF analysis framework as it allows further quantification of the exchange flow properties. It can be furthermore easily applied to any estuarine exchange flow.

Acknowledgments
This study was conducted within the framework of the Research Training Group ' Baltic TRANSCOAST' funded by the DFG (Deutsche Forschungsgemeinschaft) under grant number GRK 2000 (www.baltic-transcoast.uni-rostock.de) which funded Marvin lorenz and Hans Burchard. This is Baltic TRANSCOAST publication no. GRK2000/0029. Marvin Lorenz was further supported by the Leibniz strategy fonds (Strategiefonds-2018-IOW-I_Population structure). Knut Klingbeil was supported by the Collaborative Research Centre TRR 181 on Energy Transfer in Atmosphere and Ocean funded by the DFG (Project 274762653). The numerical simulations were performed with resources provided by the North-German Supercomputing Alliance (HLRN). Most of the analysis work was performed by computers financed by PROSO (FKZ: 03F0779A). All data behind the plots and additional model data can be found here (https://iowmeta.io-warnemuende.de/geonetwork/srv/eng/catalog.search#/metadata/IOW-IOWMETA-Persian GulfExchangeFlowModel-1993-2016)

References

Ahmad, F., & Sultan, S. (1991). Annual mean surface heat fluxes in the Arabian Gulf and the net heat transport through the Strait of Hormuz. *Atmosphere-Ocean*, *29*(1), 54–61.

Al Azhar, M., Temimi, M., Zhao, J., & Ghedira, H. (2016). Modeling of circulation in the Arabian Gulf and the Sea of Oman: Skill assessment and seasonal thermohaline structure. *Journal of Geophysical Research: Oceans*, *121*, 1700–1720. https://doi.org/10.1002/2015JC011038

Alessi, C. A., Hunt, H. D., & Bower, A. S. (1999). Hydrographic data from the US Naval Oceanographic Office: Persian Gulf, Southern Red Sea, and Arabian Sea 1923-1996: Woods Hole Oceanographic Institution Ma.

Alosairi, Y., Imberger, J., & Falconer, R. A. (2011). Mixing and flushing in the Persian Gulf (Arabian Gulf). *Journal of Geophysical Research*, *116*, C03029. https://doi.org/10.1029/2010JC006769

Amante, C., & Eakins, B. W. (2009). *ETOPO1 1 arc-minute global relief model: Procedures, data sources and analysis*. Boulder, Colorado, USA: US Department of Commerce, National Oceanic and Atmospheric Administration, National Environmental Satellite, Data, and Information Service, National Geophysical Data Center, Marine Geology and Geophysics Division Colorado.

Bignami, F., Marullo, S., Santoleri, R., & Schiano, M. (1995). Longwave radiation budget in the Mediterranean Sea. *Journal of Geophysical Research*, *100*(C2), 2501–2514.

Burchard, H., & Baumert, H. (1995). On the performance of a mixed-layer model based on the k-ε turbulence closure. *Journal of Geophysical Research*, *100*, 8523–8540. https://doi.org/10.1029/94JC03229

Burchard, H., & Bolding, K. (2002). *GETM: A general estuarine transport model; scientific documentation*: European Commission, Joint Research Centre, Institute for Environment and Sustainability.

Burchard, H., Bolding, K., Feistel, R., Gräwe, U., Klingbeil, K., MacCready, P., et al. (2018). The Knudsen theorem and the total exchange flow analysis framework applied to the Baltic Sea. *Progress in Oceanography*, *165*, 268–286. https://doi.org/10.1016/j.pocean.2018.04.004

Burchard, H., Bolding, K., & Villarreal, M. R. (1999). *GOTM, a General Ocean Turbulence Model: Theory, implementation and test cases*. Ispra: Space Applications Institute.

Burchard, H., Bolding, K., & Villarreal, M. R. (2004). Three-dimensional modelling of estuarine turbidity maxima in a tidal estuary. *Ocean Dynamics*, *54*, 250–265. https://doi.org/10.1007/s10236-003-0073-4

Burchard, H., Lange, X., Klingbeil, K., & MacCready, P. (2019). Mixing estimates for estuaries. *Journal of Physical Oceanography*, *49*(2), 631–648.

Chao, S.-Y., Kao, T. W., & Al-Hajri, K. R. (1992). A numerical investigation of circulation in the Arabian Gulf. *Journal of Geophysical Research*, *97*(C7), 11,219–11,236.

Chassignet, E. P., Hurlburt, H. E., Smedstad, O. M., Halliwell, G. R., Hogan, P. J., Wallcraft, A. J., et al. (2007). The HYCOM (HYbrid Coordinate Ocean Model) data assimilative system. *Journal of Marine Systems*, *65*(1), 60–83.

Döös, K., Nilsson, J., Nycander, J., Brodeau, L., & Ballarotta, M. (2012). The world ocean thermohaline circulation. *Journal of Physical Oceanography*, *42*(9), 1445–1460.

Döös, K., & Webb, D. J. (1994). The Deacon cell and the other meridional cells of the Southern Ocean. *Journal of Physical Oceanography*, *24*(2), 429–442.

Egbert, G. D., & Erofeeva, S. Y. (2002). Efficient inverse modeling of barotropic ocean tides. *Journal of Atmospheric and Oceanic Technology*, *19*(2), 183–204.

Elhakeem, A., Elshorbagy, W., & Bleninger, T. (2015). Long-term hydrodynamic modeling of the Arabian Gulf. *Marine pollution bulletin*, *94*(1-2), 19–36.

Gräwe, U., Holtermann, P., Klingbeil, K., & Burchard, H. (2015). Advantages of vertically adaptive coordinates in numerical models of stratified shelf seas. *Ocean Modelling*, *92*, 56–68.

Groeskamp, S., Griffies, S. M., Iudicone, D., Marsh, R., Nurser, A. G., & Zika, J. D. (2019). The water mass transformation framework for ocean physics and biogeochemistry. *Annual Review of Marine Science*, *11*, 271–305.

Hieronymus, M., Nilsson, J., & Nycander, J. (2014). Water mass transformation in salinity–temperature space. *Journal of Physical Oceanography*, *44*(9), 2547–2568.

Hofmeister, R., Beckers, J.-M., & Burchard, H. (2011). Realistic modelling of the exceptional inflows into the central Baltic Sea in 2003 using terrain-following coordinates. *Ocean Modelling*, *39*(3-4), 233–247.

Hofmeister, R., Burchard, H., & Beckers, J.-M. (2010). Non-uniform adaptive vertical grids for 3D numerical ocean models. *Ocean Modelling*, *33*(1), 70–86.

Jain, V., Shankar, D., Vinayachandran, P., Kankonkar, A., Chatterjee, A., Amol, P., et al. (2017). Evidence for the existence of Persian Gulf Water and Red Sea Water in the Bay of Bengal. *Climate Dynamics*, *48*(9-10), 3207–3226.

Jerlov, N. G. (1976). *Marine optics*, vol. 14. Amsterdam; New York: Elsevier.

Johns, W., Yao, F., Olson, D., Josey, S., Grist, J., & Smeed, D. (2003). Observations of seasonal exchange through the Straits of Hormuz and the inferred heat and freshwater budgets of the Persian Gulf. *Journal of Geophysical Research: Oceans*, *108*(C12), 3391. https://doi.org/10.1029/2003JC001881

Kämpf, J., & Sadrinasab, M. (2006). The circulation of the Persian Gulf: A numerical study. *Ocean Science*, *2*(1), 27–41.

Klingbeil, K., & Burchard, H. (2013). Implementation of a direct nonhydrostatic pressure gradient discretisation into a layered ocean model. *Ocean Modelling*, *65*, 64–77. https://doi.org/10.1016/j.ocemod.2013.02.002

Klingbeil, K., Lemarié, F., Debreu, L., & Burchard, H. (2018). The numerics of hydrostatic structured-grid coastal ocean models: State of the art and future perspectives. *Ocean Modelling*, *125*, 80–105. https://doi.org/10.1016/j.ocemod.2018.01.007

Klingbeil, K., Mohammadi-Aragh, M., Gräwe, U., & Burchard, H. (2014). Quantification of spurious dissipation and mixing—Discrete variance decay in a finite-volume framework. *Ocean Modelling*, *81*, 49–64. https://doi.org/10.1016/j.ocemod.2014.06.001

Knudsen, M. (1900). Ein hydrographischer Lehrsatz. *Annalen der Hydrographie und Maritimen Meteorologie*, *28*(7), 316–320.

Lorenz, M., Klingbeil, K., MacCready, P., & Burchard, H. (2019). Numerical issues of the Total Exchange Flow (TEF) analysis framework for quantifying estuarine circulation. *Ocean Science*, *15*(3), 601–614. https://doi.org/10.5194/os-15-601-2019

MacCready, P. (2011). Calculating estuarine exchange flow using isohaline coordinates. *Journal of Physical Oceanography*, *41*(6), 1116–1124.

MacCready, P., Rockwell Geyer, W., & Burchard, H. (2018). Estuarine exchange flow is related to mixing through the salinity variance budget. *Journal of Physical Oceanography*, *48*, 1375–1384.

Morvan, M., L'Hégaret, P., Carton, X., Gula, J., Vic, C., de Marez, C., et al. (2019). The life cycle of submesoscale eddies generated by topographic interactions. *Ocean Science*, *15*(6), 1531–1543. https://doi.org/10.5194/os-15-1531-2019

Pietrzak, J. (1998). The use of TVD limiters for forward-in-time upstream-biased advection schemes in ocean modeling. *Monthly Weather Review*, *126*(3), 812–830.

Pous, S., Carton, X., & Lazure, P. (2004). Hydrology and circulation in the Strait of Hormuz and the Gulf of OmanResults from the GOGP99 experiment: 1. Strait of Hormuz. *Journal of Geophysical Research*, *109*, C12037. https://doi.org/10.1029/2003JC002145

Pous, S., Carton, X., & Lazure, P. (2012). A process study of the tidal circulation in the Persian Gulf. *Open Journal of Marine Science*, *2*(4), 131–140.

Pous, S., Lazure, P., & Carton, X. (2015). A model of the general circulation in the Persian Gulf and in the Strait of Hormuz: Intraseasonal to interannual variability. *Continental Shelf Research*, *94*, 55–70.

Privett, D. (1959). Monthly charts of evaporation from the N. Indian Ocean (including the Red Sea and the Persian Gulf). *Quarterly Journal of the Royal Meteorological Society*, *85*(366), 424–428.

Reynolds, R. M. (1993). Physical oceanography of the Gulf, Strait of Hormuz, and the Gulf of OmanResults from the Mt Mitchell expedition. *Marine Pollution Bulletin*, *27*, 35–59.

Reynolds, R. W., Smith, T. M., Liu, C., Chelton, D. B., Casey, K. S., & Schlax, M. G. (2007). Daily high-resolution-blended analyses for sea surface temperature. *Journal of Climate*, *20*(22), 5473–5496.

Rodi, W. (1987). Examples of calculation methods for flow and mixing in stratified fluids. *Journal of Geophysical Research*, *92*, 5305–5328. https://doi.org/10.1029/JC092iC05p05305

Saha, S., Moorthi, S., Pan, H.-L., Wu, X., Wang, J., Nadiga, S., et al. (2010). *NCEP Climate Forecast System Reanalysis (CFSR) Selected Hourly Time-Series Products, January 1979 to December 2010*. Boulder CO. https://doi.org/10.5065/D6513W89

Saha, S., Moorthi, S., Wu, X., Wang, J., Nadiga, S., Tripp, P., et al. (2011). *NCEP climate forecast system version 2 (CFSv2) selected hourly time-series products*. Boulder CO: Research Data Archive at the National Center for Atmospheric Research, Computational and Information Systems Laboratory. https://doi.org/10.5065/D6N877VB

Shchepetkin, A. F., & McWilliams, J. C. (2003). A method for computing horizontal pressure-gradient force in an oceanic model with a nonaligned vertical coordinate. *Journal of Geophysical Research*, *108*(C3), 3090. https://doi.org/10.1029/2001JC001047

Smagorinsky, J. (1963). General circulation experiments with the primitive equations: I. The basic experiment. *Monthly Weather Review*, *91*(3), 99–164.

Smirnov, A., Holben, B. N., Dubovik, O., O'Neill, N. T., Eck, T. F., Westphal, D. L., et al. (2002). Atmospheric aerosol optical properties in the Persian Gulf. *Journal of the Atmospheric Sciences*, *59*(3), 620–634.

Speer, K. G. (1993). Conversion among North Atlantic surface water types. *Tellus A*, *45*(1), 72–79.

Stark, J. D., Donlon, C. J., Martin, M. J., & McCulloch, M. E. (2007). OSTIA: An operational, high resolution, real time, global sea surface temperature analysis system. In *Oceans 2007-europe*, pp. 1–4.

Swift, S. A., & Bower, A. S. (2003). Formation and circulation of dense water in the Persian/Arabian Gulf. *Journal of Geophysical Research*, *108*(C1), 3004. https://doi.org/10.1029/2002JC001360

Thoppil, P. G., & Hogan, P. J. (2009). On the mechanisms of episodic salinity outflow events in the Strait of Hormuz. *Journal of Physical Oceanography*, *39*(6), 1340–1360.

Thoppil, P. G., & Hogan, P. J. (2010). A modeling study of circulation and eddies in the Persian Gulf. *Journal of Physical Oceanography*, *40*(9), 2122–2134.

Tragou, E., Garrett, C., Outerbridge, R., & Gilman, C. (1999). The heat and fresh water budgets of the Red Sea. *Journal of Physical Oceanography*, *29*(10), 2504–2522.

Umlauf, L., & Burchard, H. (2005). Second-order turbulence closure models for geophysical boundary layers. A review of recent work. *Continental Shelf Research*, *25*(7-8), 795–827.

Vic, C., Roullet, G., Capet, X., Carton, X., Molemaker, M. J., & Gula, J. (2015). Eddy-topography interactions and the fate of the Persian Gulf Outflow. *Journal of Geophysical Research: Oceans*, *120*, 6700–6717. https://doi.org/10.1002/2015JC011033

Walin, G. (1977). A theoretical framework for the description of estuaries. *Tellus*, *29*, 128–136.

Walin, G. (1982). On the relation between sea-surface heat flow and thermal circulation in the ocean. *Tellus*, *34*(2), 187–195.

Willmott, C. J. (1981). On the validation of models. *Physical Geography*, *2*(2), 184–194.

Willmott, C. J. (1982). Some comments on the evaluation of model performance. *Bulletin of the American Meteorological Society*, *63*(11), 1309–1313.

Worthington, L. (1981). 2 the water masses of the world ocean: Some results of a fine-scale census.

Yao, F., & Johns, W. E. (2010a). A HYCOM modeling study of the Persian Gulf: 1. Model configurations and surface circulation. *Journal of Geophysical Research*, *115*, C11017. https://doi.org/10.1029/2009JC005781

Yao, F., & Johns, W. E. (2010b). A HYCOM modeling study of the Persian Gulf: 2. Formation and export of Persian Gulf Water. *Journal of Geophysical Research*, *115*, C11018. https://doi.org/10.1029/2009JC005788

Zika, J. D., Sijp, W. P., & England, M. H. (2013). Vertical heat transport by ocean circulation and the role of mechanical and haline forcing. *Journal of Physical Oceanography*, *43*(10), 2095–2112.